NASA TECHNICAL NOTE

NASA TN D-4558

NASA TN D-4558

DYNAMIC STABILITY OF A 4.6-METER-DIAMETER 120° CONICAL SPACECRAFT AT MACH NUMBERS FROM 0.78 TO 0.48 IN A SIMULATED MARTIAN ENVIRONMENT

by Charles H. Whitlock and Richard J. Bendura

Langley Research Center
Langley Station, Hampton, Va.

NATIONAL AERONAUTICS AND SPACE ADMINISTRATION • WASHINGTON, D. C. • MAY 1968

DYNAMIC STABILITY OF A 4.6-METER-DIAMETER 120° CONICAL SPACECRAFT AT MACH NUMBERS FROM 0.78 TO 0.48 IN A SIMULATED MARTIAN ENVIRONMENT

By Charles H. Whitlock and Richard J. Bendura

Langley Research Center
Langley Station, Hampton, Va.

NATIONAL AERONAUTICS AND SPACE ADMINISTRATION

For sale by the Clearinghouse for Federal Scientific and Technical Information
Springfield, Virginia 22151 – CFSTI price $3.00

DYNAMIC STABILITY OF A 4.6-METER-DIAMETER 120° CONICAL SPACECRAFT AT MACH NUMBERS FROM 0.78 TO 0.48 IN A SIMULATED MARTIAN ENVIRONMENT

By Charles H. Whitlock and Richard J. Bendura
Langley Research Center

SUMMARY

Subsonic dynamic stability characteristics of a large-size 120° conical spacecraft have been determined from flight data in a simulated Martian environment. The results cover a Mach number range from 0.78 to 0.48, and a Reynolds number range from 200 000 to 100 000 (based on 15-foot (4.6 meter) spacecraft diameter). Assumptions of the analysis include linear static aerodynamics and invariant dynamic stability derivative $C_{m_q} + C_{m_{\dot{\alpha}}}$ with angle of attack. Reduction of the data on a cycle-by-cycle basis gives $C_{m_q} + C_{m_{\dot{\alpha}}}$ values near -0.135 with an uncertainty of ±0.105 over the range of the test. Trajectory simulation studies indicate that a reasonable simulation can be obtained by using a damping coefficient of -0.135, and that ±0.105 is a realistic value for the accuracy limit.

INTRODUCTION

Large-angle blunted cones are being considered as configurations for entry into planetary atmospheres. A blunt 120° total angle conical shape is proposed for several future programs and was used for the Planetary Entry Parachute Program. The dynamic stability characteristics of this shape are under investigation in ground facilities. References 1 and 2 present dynamic stability derivative $\left(C_{m_q} + C_{m_{\dot{\alpha}}}\right)$ data for both low subsonic and hypersonic velocities on small-scale models. The purpose of this report is to present the dynamic stability characteristics of a large-size 120° conical spacecraft determined from free-flight data at Mach number and Reynolds number conditions that simulate a possible Martian environment.

The results were obtained from the first flight test of the balloon-launched series of the Planetary Entry Parachute Program. Details of the flight are described in references 3 and 4. By utilizing the spacecraft attitude histories obtained in reference 5,

values for the dynamic stability derivative $C_{m_q} + C_{m_{\dot{\alpha}}}$ are obtained at Mach numbers from 0.78 to 0.48 at earth altitudes between 138 000 feet (42.1 kilometers) and 143 000 feet (43.6 kilometers). Reynolds number (based on the 15-foot (4.6 meter) spacecraft diameter) varied from 200 000 to 100 000.

SYMBOLS

$[B]$ transformation matrix defined in equation (1)

C_A axial-force coefficient (positive rearward), $\frac{\text{Axial force}}{q'S}$

C_m pitching-moment coefficient, $\frac{\text{Pitching moment}}{q'SD}$

$C_{m_q} = \frac{\partial C_m}{\partial (qD/2V')}$, per radian

C_{m_α} pitching-moment-curve slope, $\frac{\partial C_m}{\partial \alpha}$, per radian

$C_{m_{\dot{\alpha}}} = \frac{\partial C_m}{\partial (\dot{\alpha}D/2V')}$, per radian

C_N normal-force coefficient, $\frac{\text{Normal force}}{q'S}$

C_{N_α} normal-force-curve slope, $\frac{\partial C_N}{\partial \alpha}$, per radian

D maximum body diameter, feet (meters)

I moment of inertia about pitch or yaw axis, slugs-feet^2 (kilograms-meters^2)

I_X moment of inertia about roll axis, slugs-feet^2 (kilograms-meters^2)

m mass of spacecraft, slugs (kilograms)

p,q,r roll, pitch, and yaw velocities, respectively, radians/second

q' free-stream dynamic pressure, pounds force/foot^2 (newtons/meter^2)

S maximum cross-sectional area of body, feet^2 (meters^2)

t	time from spacecraft separation, seconds
t'	time to one-half amplitude of corrected angle-of-attack ratio squared, seconds
u,v,w	component of spacecraft linear velocity relative to earth along X-, Y-, and Z-axis, respectively, feet/second (meters/second)
u',v',w'	component of spacecraft linear velocity relative to wind along X-, Y-, and Z-axis, respectively, feet/second (meters/second)
V'	free-stream velocity, feet/second (meters/second)
$V_{w,XE},V_{w,YE},V_{w,ZE}$	wind velocity component along X_E-, Y_E-, and Z_E-axis, respectively
X,Y,Z	body axes of spacecraft
X_E,Y_E,Z_E	earth-fixed axes
$\dot{X}_E,\dot{Y}_E,\dot{Z}_E$	spacecraft velocity components along X_E-, Y_E-, and Z_E-axis, respectively
x_{cg}	center-of-gravity distance rearward from apex, feet (meters)
α,β	angles of attack in pitch and yaw, respectively, degrees
η	resultant angle of attack, degrees
θ,ϕ,ψ	pitch, roll, and yaw angles of spacecraft relative to earth-fixed axes, respectively, radians or degrees
ρ	atmospheric density, slugs/foot^3 (kilograms/meter^3)
γ_p	flight-path angle in pitch, degrees
γ_y	flight-path angle in yaw, degrees
λ_o	damping parameter, $\frac{-0.693}{2t'}$

Dots over symbols indicate derivatives with respect to time.

CONFIGURATION AND TEST ENVIRONMENT

A sketch of the spacecraft configuration utilized for the first flight of the balloon-launched series of the Planetary Entry Parachute Program is shown in figure 1. The mission profile is shown in figure 2. The results described herein were obtained during the aeroshell coast portion of flight which occurred after parachute deployment and subsequent aeroshell separation from the payload. The center-of-gravity location shown in figure 1 is that after aeroshell separation. Mass properties are as follows:

m	21.68 slugs (316.4 kg)
x_{cg}/D, rearward from apex	0.218
I_X	203 slugs-ft^2 (275 kg-m^2)
I	159 slugs-ft^2 (215 kg-m^2)

Mass and center of gravity are measured values. Roll inertia was estimated, and pitch-yaw inertia is an average value deduced from observed motion frequencies and wind-tunnel values for C_{m_α}. The Euler angle and aerodynamic angle system used in this analysis are those of reference 6. Figure 3 is a sketch showing the two systems.

In terms of flight time, aeroshell separation occurred at approximately 14 seconds from spacecraft release and attitude data were obtained from onboard motion-picture cameras until 27.3 seconds of the release. Beyond this time, sight of the earth was lost by the rearward-facing cameras as the aeroshell approached apogee. Time histories of the Euler angles (θ, ψ, and ϕ) are shown in figures 4, 5, and 6 (from ref. 5). Figure 4 shows the θ time history obtained from both cameras 1 and 2, and the ψ and ϕ time histories are shown in figures 5 and 6, respectively. The Mach number and dynamic pressure histories during the data period are shown in figure 7. It should be noted that the dynamic pressure decreased (from 2.1 pounds per square foot (100.5 N/m^2) initially) by a factor of 3.28 during the data period. Reynolds number varied from 200 000 to 100 000 based on spacecraft diameter.

ANALYSIS AND RESULTS

From the results of reference 5, values for the dynamic stability derivative $C_{m_q} + C_{m_{\dot\alpha}}$ are determined in the data-reduction section which follows. The validity of the results is tested by use of trajectory simulation techniques in a subsequent section.

Data Reduction

If the spacecraft attitude angles θ, ϕ, and ψ are known, free-stream velocity components along the body X-, Y-, and Z-axes can be calculated by use of the following equation:

$$\begin{Bmatrix} u' \\ v' \\ w' \end{Bmatrix} = \begin{Bmatrix} u' \\ v' \\ w' \end{Bmatrix} = [B] \begin{Bmatrix} \dot{X}_E \\ \dot{Y}_E \\ \dot{Z}_E \end{Bmatrix} - [B] \begin{Bmatrix} V_{w,XE} \\ V_{w,YE} \\ V_{w,ZE} \end{Bmatrix} \tag{1}$$

where

$$[B] = \begin{bmatrix} (\cos\theta \sin\psi) & (\cos\theta \sin\psi) & (-\sin\theta) \\ (\cos\psi \sin\theta \sin\phi - \sin\psi \cos\phi) & (\cos\psi \cos\phi + \sin\psi \sin\theta \sin\phi) & (\cos\theta \sin\phi) \\ (\cos\psi \sin\theta \cos\phi + \sin\psi \sin\phi) & (\sin\psi \sin\theta \cos\phi - \cos\psi \sin\phi) & (\cos\theta \cos\phi) \end{bmatrix}$$

The earth-relative velocities $\dot{X}_E$, $\dot{Y}_E$, and $\dot{Z}_E$ were determined from ground-track data. Wind velocities were obtained by means of an Arcasonde sounding rocket which was launched 1 hour after spacecraft release. Location of the Arcasonde during descent was within 20 miles of the aeroshell during the data period. It was assumed that the winds measured by the Arcasonde were those that existed during aeroshell flight. The wind velocity in the vertical direction $V_{w,ZE}$ was assumed to be zero. If the free-stream velocity components are known, spacecraft angles of attack can be calculated by use of the following relations (see fig. 3):

$$\alpha = \tan^{-1} \frac{w'}{u'} \tag{2}$$

$$\beta = \tan^{-1} \frac{v'}{u'} \tag{3}$$

$$\eta = \tan^{-1} \frac{\sqrt{v'^2 + w'^2}}{u'} \tag{4}$$

Figure 8 shows the η time history, and figure 9 shows the α,β crossplot for each camera. The fairing of curves between the data points in figure 8 was accomplished by utilizing the cross plots in figure 9. Average envelopes enclosing the η histories were also faired. The first peak on the camera 1 results was ignored because based on a detailed review of data used in reference 5, the point at 15.56 seconds was believed to contain greater than average error. Differences between the values obtained by the two cameras are attributed primarily to two sources of error. First, the basic method of obtaining the Euler angles from photographs is subject to error (see ref. 5), and second, it was established that the two cameras were misalined relative to each other and to the

longitudinal axis of the spacecraft. Camera misalinement would show up as a trim angle on the α,β crossplot. Examination of figure 9 shows camera 1 yawed relative to camera 2, but it is not known which camera is more closely alined with either the aeroshell trim or longitudinal axis (which may not coincide). However, based on figure 9, the misalinements between either camera and the trim axis appear to be small (less than 5°).

In order to establish whether the spacecraft was stable or unstable, it was necessary to consider the general nature of the η history. It has been generally observed (ref. 7, for example) that the amplitude ratio of the oscillatory motion varies inversely as the fourth root of the dynamic pressure ratio if C_{m_α} does not vary with Mach number, the spacecraft roll rate is small, and there is no aerodynamic damping. Static stability data derived from wind-tunnel results (shown in fig. 10) and the roll history in figure 6 indicate that the first two assumptions are reasonable in this case. Also a trajectory simulation of the test verified that the resultant angle-of-attack ratio did follow the inverse of the fourth root of the dynamic pressure ratio if no damping is present. As noted previously, both the dynamic pressure and Mach number varied during the data period. If the spacecraft contained no aerodynamic damping, the amplitude of η would have increased by a factor of 1.33 during the time period 14.3 to 25.9 seconds based on the dynamic pressure history. The camera 1 results would have an amplitude of 32°, and the camera 2 data would show a peak of 36.6° at 25.9 seconds if no damping were present. Since neither amplitude increased by the factor of 1.33 (fourth root of the dynamic pressure ratio), it is concluded that the spacecraft did contain positive damping $\left(\text{negative } C_{m_q} + C_{m_{\dot\alpha}}\right)$ during the data period.

To evaluate the magnitude of $C_{m_q} + C_{m_{\dot\alpha}}$, the methods of reference 8 were used after a correction to account for the variable dynamic pressure was applied. Assumptions of the analysis include linear static aerodynamics and constant $C_{m_q} + C_{m_{\dot\alpha}}$ with angle of attack. Also the effects of trim were neglected. For each cycle the measured resultant angle-of-attack ratio squared was corrected by the square root of the inverse of the dynamic pressure ratio, and the damping parameter λ_o was calculated by use of the relation

$$\lambda_o = -\frac{0.693}{2t'} \tag{5}$$

where t' is the time to one-half amplitude of the corrected resultant angle-of-attack ratio squared (taken from similar log plots as shown in ref. 8). Damping derivatives were calculated for each cycle at an average Mach number from the relation

$$C_{m_q} + C_{m_{\dot\alpha}} = \frac{2I}{mD^2}\left(\frac{4m}{\rho S V'}\lambda_o + C_{N_\alpha}\right)$$

The damping observed is assumed to include the effects of $C_{m_{\dot{\alpha}}}$ as well as those of C_{m_q}. Average values during each cycle for the parameter $4m/\rho SV'$ were used. The results of these calculations are shown in figure 11 at the average Mach number for each cycle. Also shown are the estimated uncertainty based on extreme fairings of the η envelopes, the uncertainty in inertia properties, and the possible errors in dynamic pressure values. Wind velocities were to the order of 120 feet per second (36.6 meters per second), and an uncertainty of 20 feet per second (6.1 meters per second) must be considered in the final reduced values. The estimated uncertainty in $C_{m_q} + C_{m_{\dot{\alpha}}}$ appears large when considered in terms of magnitude, but when compared with ballistics range results shown in reference 2, the flight test uncertainties appear reasonable.

Trajectory Simulation

In order to verify the general amplitude of the calculated $C_{m_q} + C_{m_{\dot{\alpha}}}$ values, the flight trajectory was simulated on an IBM 7094 electronic data processing machine by using the six-degrees-of-freedom program described in reference 6. For brevity, the results from only camera 1 were considered. It was realized that a precise simulation would not be possible because of uncertainties in the spacecraft inertial properties and wind conditions used as program inputs. Also the Euler angle histories being simulated were subject to some error. (See ref. 5.) By considering the general level of $C_{m_q} + C_{m_{\dot{\alpha}}}$, however, it was believed that the general nature of the motion could be simulated. By use of outside bounds for $C_{m_q} + C_{m_{\dot{\alpha}}}$, it was expected that the estimated uncertainty values could also be substantiated .

Review of the data in figure 11 indicates that values of -0.03 and -0.24 represent outside bounds of $C_{m_q} + C_{m_{\dot{\alpha}}}$ if Mach number effects are neglected. The average of these two values, -0.135, was selected for use in initial simulations to verify the general level of $C_{m_q} + C_{m_{\dot{\alpha}}}$. Mass properties and static aerodynamics (fig. 10) discussed previously were used. The initial conditions required were: (1) spacecraft position $(X_E, Y_E, \text{and } Z_E)$; (2) spacecraft attitude (θ, ϕ, and ψ); (3) spacecraft velocity components relative to earth along body X-, Y-, and Z-axes (u, v, and w); and (4) spacecraft roll, pitch, and yaw velocities (p, q, and r). At an initial time of 14.17 seconds, spacecraft position was obtained from ground-tracking data, and attitude was taken from figures 4 to 6. Velocity components along the body axes relative to Earth were calculated from

$$\begin{Bmatrix} u \\ v \\ w \end{Bmatrix} = [B] \begin{Bmatrix} \dot{X}_E \\ \dot{Y}_E \\ \dot{Z}_E \end{Bmatrix} \tag{6}$$

Initial roll, pitch, and yaw velocities were obtained from the relations:

$$\left.\begin{aligned} p &= \dot{\phi} - \dot{\psi} \sin \theta \\ q &= \dot{\theta} \cos \phi + \dot{\psi} \cos \theta \sin \phi \\ r &= -\dot{\theta} \sin \phi + \dot{\psi} \cos \theta \cos \phi \end{aligned}\right\} \qquad (7)$$

The simulation process consisted of successive iteration to determine the combination of initial conditions and aerodynamic trim angle which provided the best simulation of the flight Euler angle histories. After initial calculations with equation (7), the values for p, q, and r were adjusted slightly to provide a good simulation for the first-quarter cycle of motion (before damping could be effective). Then the effects of various trim angles were investigated until a combination which provided motions that were centered about and in phase with the flight θ and ψ histories was found. (Some readjustment of p, q, and r was necessary to simulate the first quarter cycle.) Finally, the initial value of $C_{m_q} + C_{m_{\dot{\alpha}}}$ (-0.135) was changed first to -0.03 and then to -0.24 to determine the effects of the estimated accuracy limits on the spacecraft motions.

The final initial conditions used in the simulation are:

t, seconds	14.17
X_E, feet (meters)	0 (0)
Y_E, feet (meters)	0 (0)
Z_E, feet (meters)	-136 150 (-41 499)
θ, radians	0.488
ϕ, radians	4.42
ψ, radians	2.78
u, feet per second (meters per second)	691 (211)
v, feet per second (meters per second)	333 (101)
w, feet per second (meters per second)	-23 (-7)
p, radians per second	0.26
q, radians per second	0.25
r, radians per second	-0.35

The aerodynamic trim angles which gave the best overall results were

$$\alpha_{trim} = 0.6^{o}$$

$$\beta_{trim} = -1.9^{o}$$

The final values for p, q, and r were changes from 0.312 rad/sec, 0.912 rad/sec, and -0.298 rad/sec which were the respective values used in initial simulations. Changes were necessary because of inaccuracies caused by taking slopes of θ, ϕ, and ψ for use in equations (7); and by the fact that each time the trim angle was varied, q and r had to be readjusted to simulate the first-quarter cycle of motion.

The values of θ, ψ, and ϕ from the best simulation with $C_{m_q} + C_{m_{\dot{\alpha}}} = -0.135$ are compared with the flight data in figure 12. A precise simulation could not be obtained with constant aerodynamics and mass properties. The low-amplitude oscillations of θ and ψ are not duplicated. The large-amplitude motions are in good agreement; hence, the η history is expected to be a reasonable simulation of the flight conditions. Comparison of the simulation and flight values of η in figure 13 substantiates this conclusion. The inability to simulate the low-amplitude motions is probably caused by errors in the inertia values used, the possibility of nonsymmetric pitch and yaw inertias, and the probability of products of inertia in the flight vehicle. Also the previously discussed uncertainty in the wind profile used in the simulation is a source of error. The α,β crossplot from the simulation is shown in figure 14. The width of the loops and the low-amplitude values of η do not agree with the camera 1 results in figure 9. Comparison of the flight and simulation motion patterns with the typical motion patterns (below roll resonance) in reference 8 suggests that slight errors in the inertia properties are the most probable cause for the inability to simulate the motion patterns. Error in the calculated values of $C_{m_q} + C_{m_{\dot{\alpha}}}$ due to inertia uncertainties is expected to be small, however, because the oscillation frequencies correlate and indicate that the pitch and yaw inertias are in the right range. If figure 13 is compared with figure 8, it appears that the overall trend of the simulated η history is in good agreement with the motion characteristics deduced from both sets of camera data. It is concluded that a reasonable simulation of the flight motions could be obtained with $C_{m_q} + C_{m_{\dot{\alpha}}} = -0.135$.

Simulated trajectories were also computed by using $C_{m_q} + C_{m_{\dot{\alpha}}}$ equal to -0.03 and -0.24 in order to test the accuracy limits established during data reduction. The same initial conditions and trim angles as described previously were used so that the first-quarter cycle of motion was simulated. The results of these computations are shown in figures 15 and 16. Figure 15 shows θ, ψ, and ϕ histories for both values of $C_{m_q} + C_{m_{\dot{\alpha}}}$ along with the flight data points. Variation of $C_{m_q} + C_{m_{\dot{\alpha}}}$ does not significantly affect the low-amplitude values of θ or ψ which were not well simulated in the first place. In general, minimum damping appears to cause excessive amplitudes, and maximum $C_{m_q} + C_{m_{\dot{\alpha}}}$ causes the simulation to begin to peak beneath the high-amplitude values during the latter portion of the data period. These same trends are evident from the comparison of the η histories shown in figure 16. The low-damping simulation causes excessive divergence, and the high-damping case maintains nearly

constant amplitude. The best fairings of flight data in figure 8 show a slight divergence; hence, it is concluded that -0.03 and -0.24 are reasonable accuracy limits.

CONCLUDING REMARKS

Dynamic stability derivatives were obtained from the flight test of a 4.6-meter-diameter 120° conical spacecraft in a simulated Martian environment. Comparison of the rate of divergence of the resultant angle-of-attack η histories with predictions based on the dynamic pressure history indicate positive damping during the data period. Actual reduction of the data on a cycle-by-cycle basis by using faired η envelopes gives dynamic stability derivative $\left(C_{m_q} + C_{m_{\dot{\alpha}}}\right)$ values near -0.135 in the Mach number range from 0.78 to 0.48. An estimated uncertainty of ±0.105 is based on extreme fairings of the η history, possible errors in the inertia values, and inaccuracies in the wind data. Trajectory simulation studies indicate that a reasonable simulation can be obtained by using a damping coefficient of -0.135 and that ±0.105 is a realistic value for the accuracy limit.

Langley Research Center,
National Aeronautics and Space Administration,
Langley Station, Hampton, Va., January 19, 1968,
124-07-03-05-23.

REFERENCES

1. Bendura, Richard J.: Low Subsonic Static and Dynamic Stability Characteristics of Two Blunt 120° Cone Configurations. NASA TN D-3853, 1967.

2. Krumins, Maigonis V.: A Ballistic Range Study of Aerodynamic Characteristics of Mars Probe/Lander Shapes. Paper No. 67-167, Amer. Inst. Aeron. Astronaut., Jan. 1967.

3. Darnell, Wayne L., Henning, Allen B., and Lundstrom, Reginald R.: Flight Test of a 15-Foot Diameter (4.6-Meter) 120° Conical Spacecraft Simulating Parachute Deployment in a Mars Atmosphere. NASA TN D-4266, 1967.

4. Whitlock, Charles H.; Bendura, Richard J.; and Coltrane, Lucille C.: Performance of a 26-Meter-Diameter Ringsail Parachute in a Simulated Martian Environment. NASA TM X-1356, 1967.

5. Bendura, Richard J.; Henning, Allen B.; and Smith, Robert E., Jr.: Vehicle Attitude Determination With a Single Onboard Camera. NASA TN D-4359, 1968.

6. James, Robert L., Jr. (With Appendix by Crabill, Norman L.): A Three-Dimensional Trajectory Simulation Using Six Degrees of Freedom With Arbitrary Wind. NASA TN D-641, 1961.

7. Nicolaides, John D.; Eikenberry, Robert S.; and Ingram, Charles W.: The Determination of Aerodynamic Stability Coefficients From Sounding Rocket Flight Data. AIAA Sounding Rocket Vehicle Technology Specialist Conference, Feb.-Mar. 1967, pp. 257-270.

8. Nelson, Robert L.: The Motions of Rolling Symmetrical Missiles Referred to a Body-Axis System. NACA TN 3737, 1956.

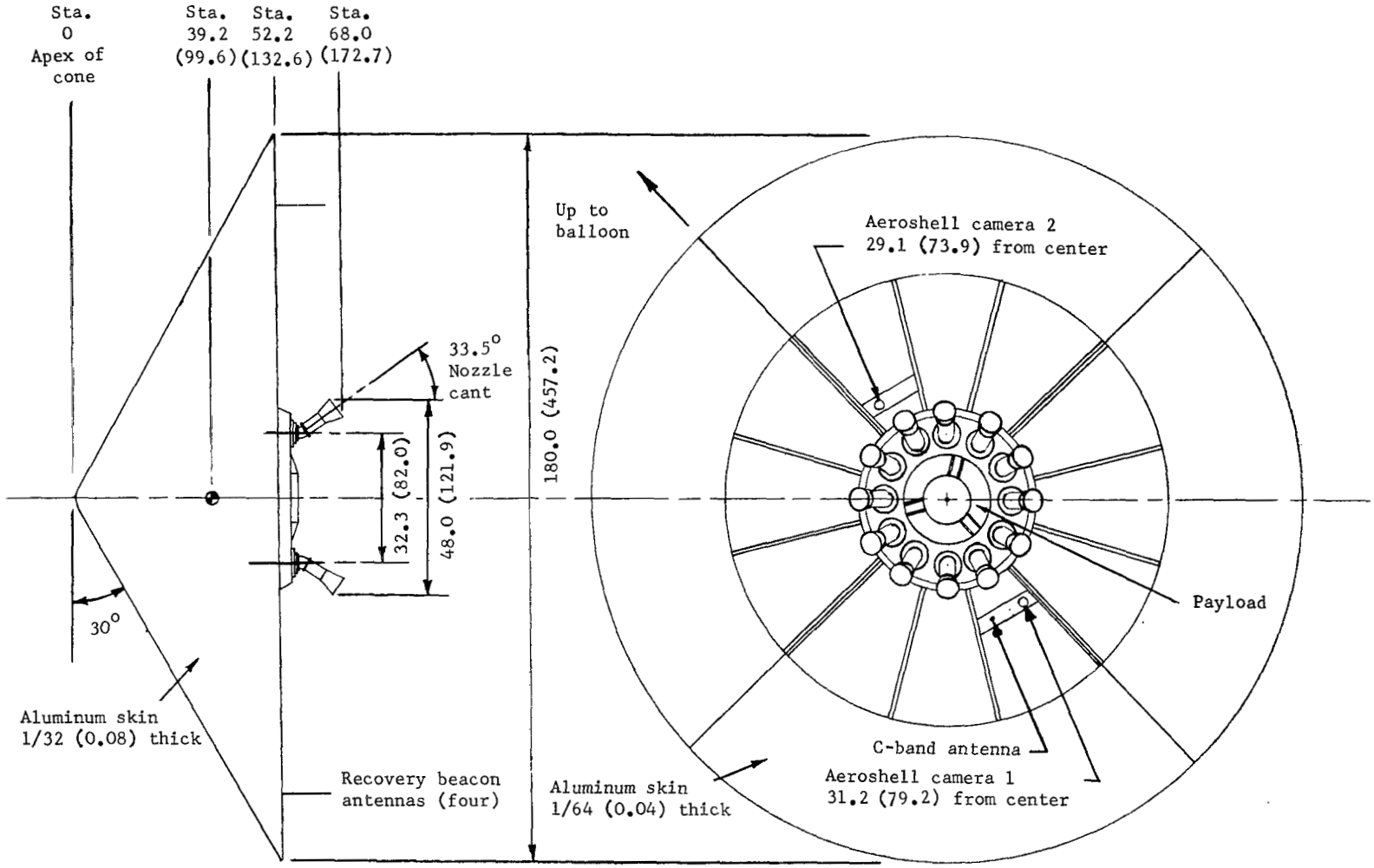

Figure 1.- Side- and rear-view sketch of spacecraft. All dimensions and stations are in inches (cm).

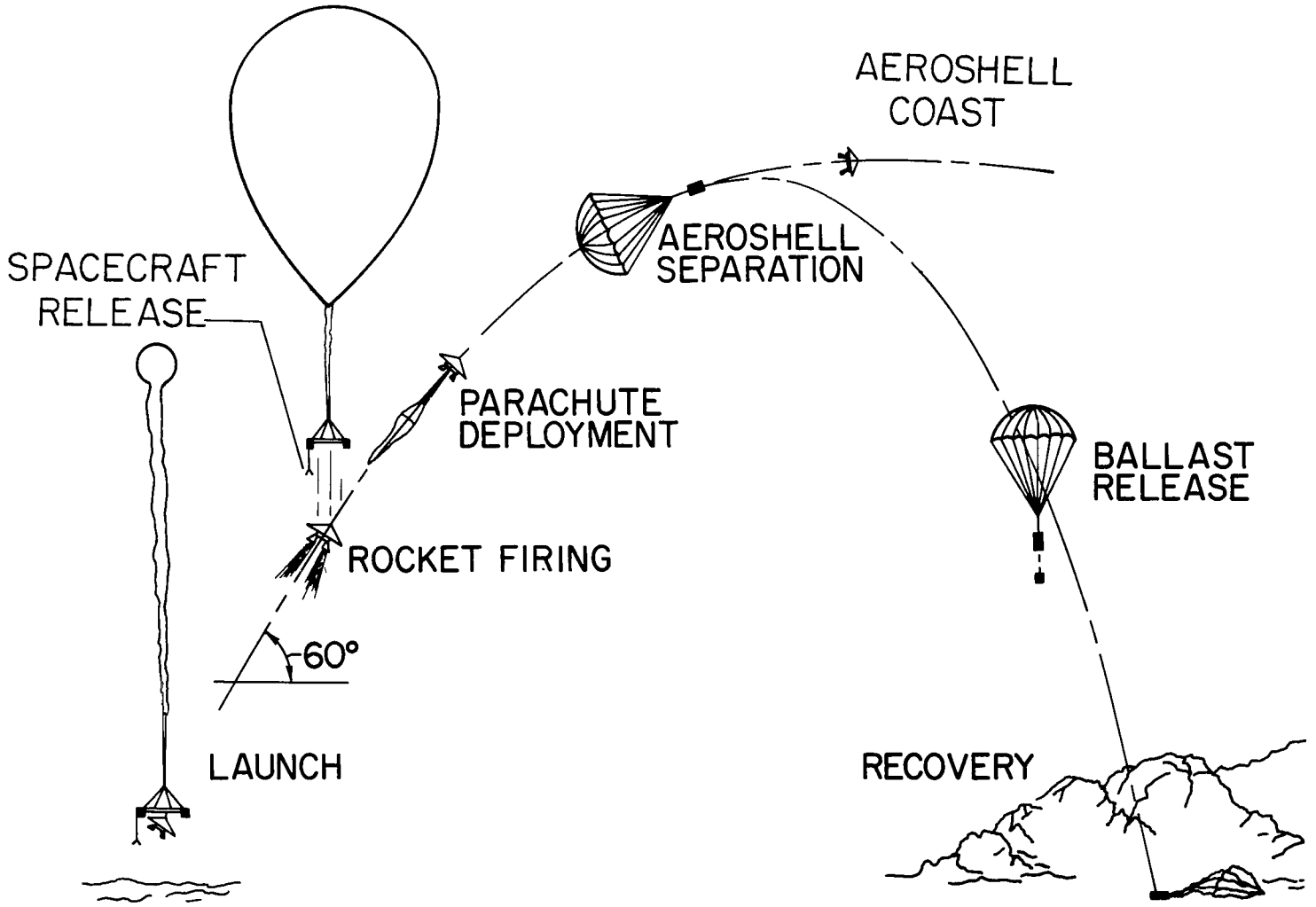

Figure 2.- Mission profile.

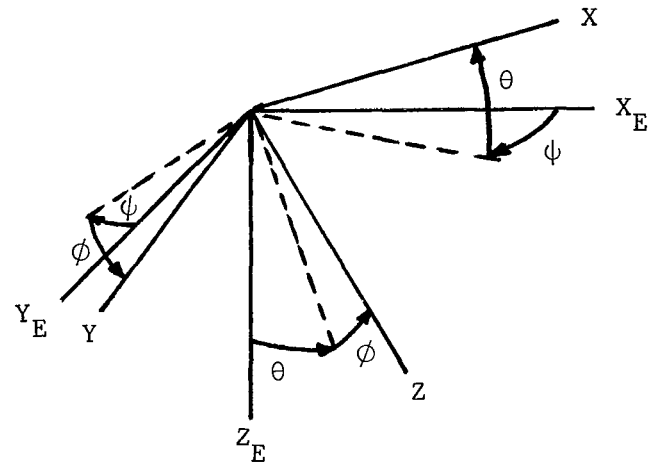

(a) Euler angle system.

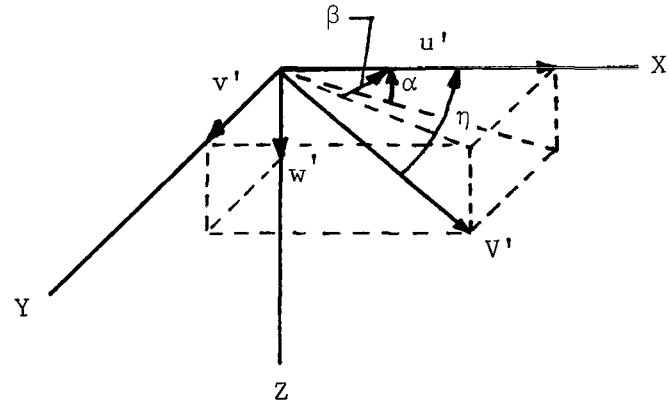

(b) Aerodynamic angle system.

Figure 3.- Body-axis system orientation.

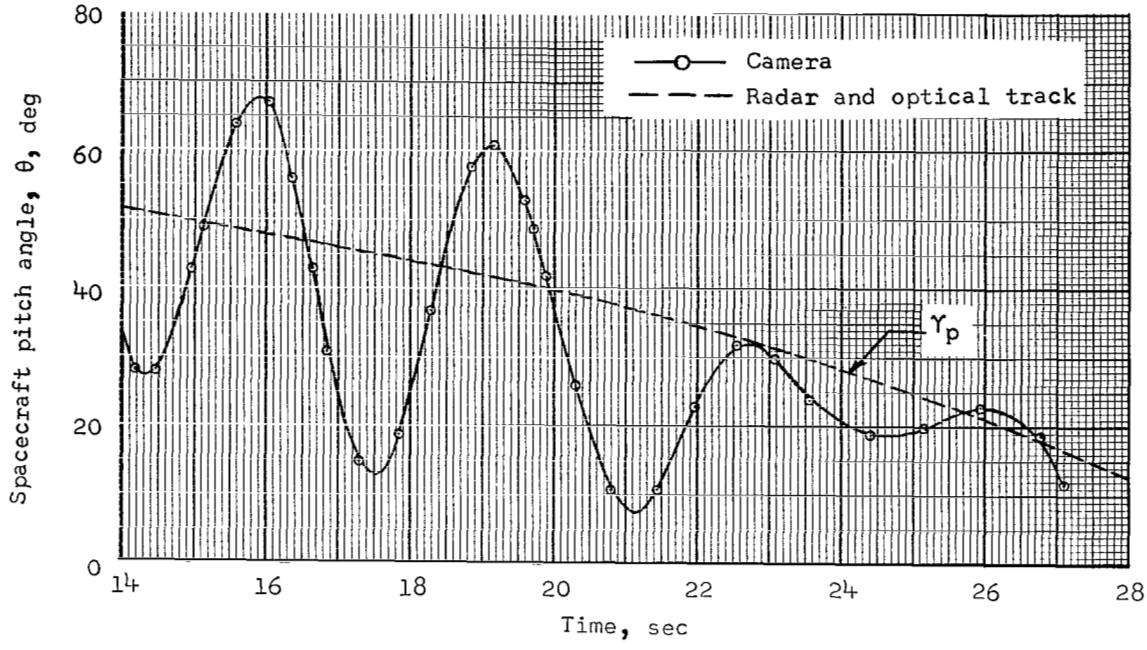

(a) Camera 1.

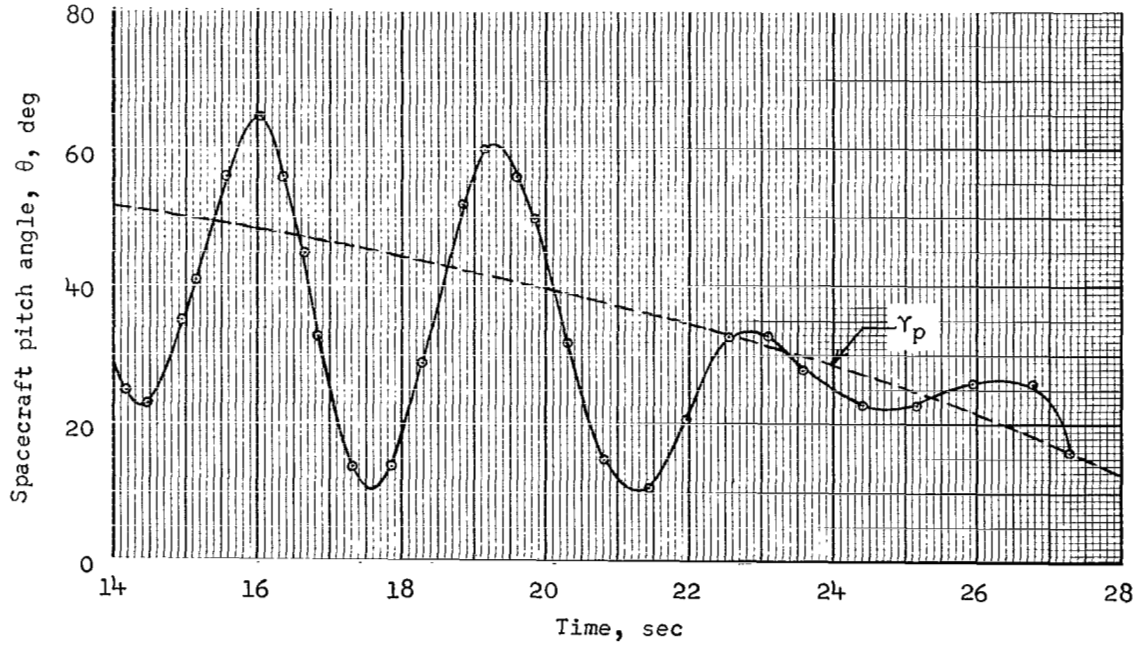

(b) Camera 2.

Figure 4.- Pitch-angle time history.

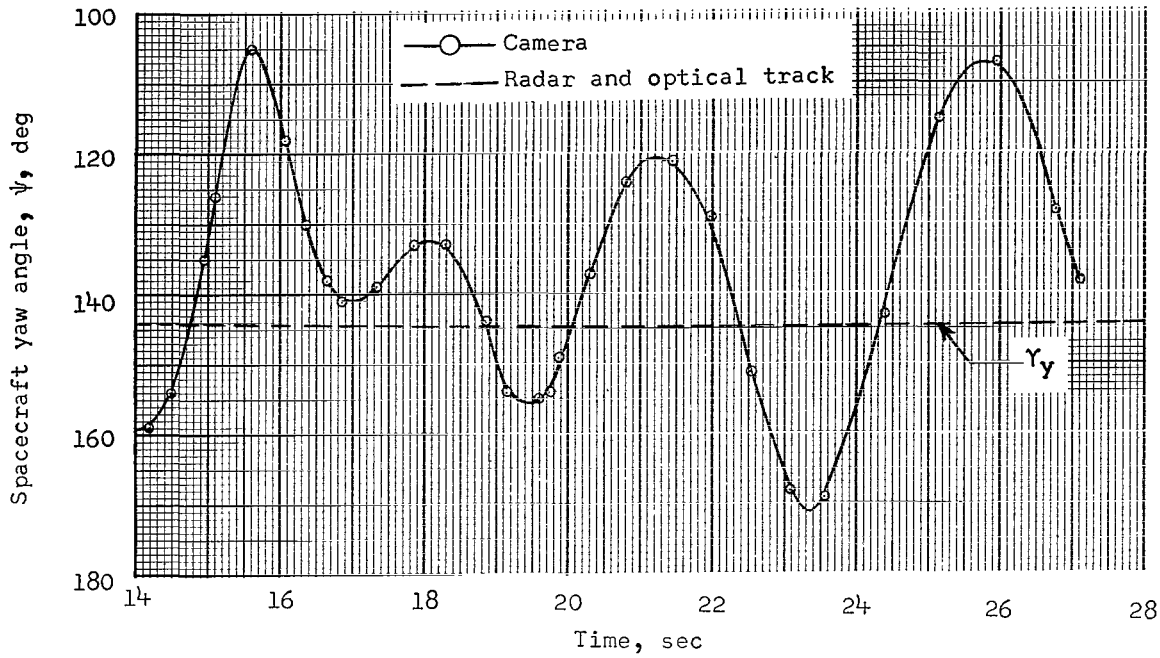

(a) Camera 1.

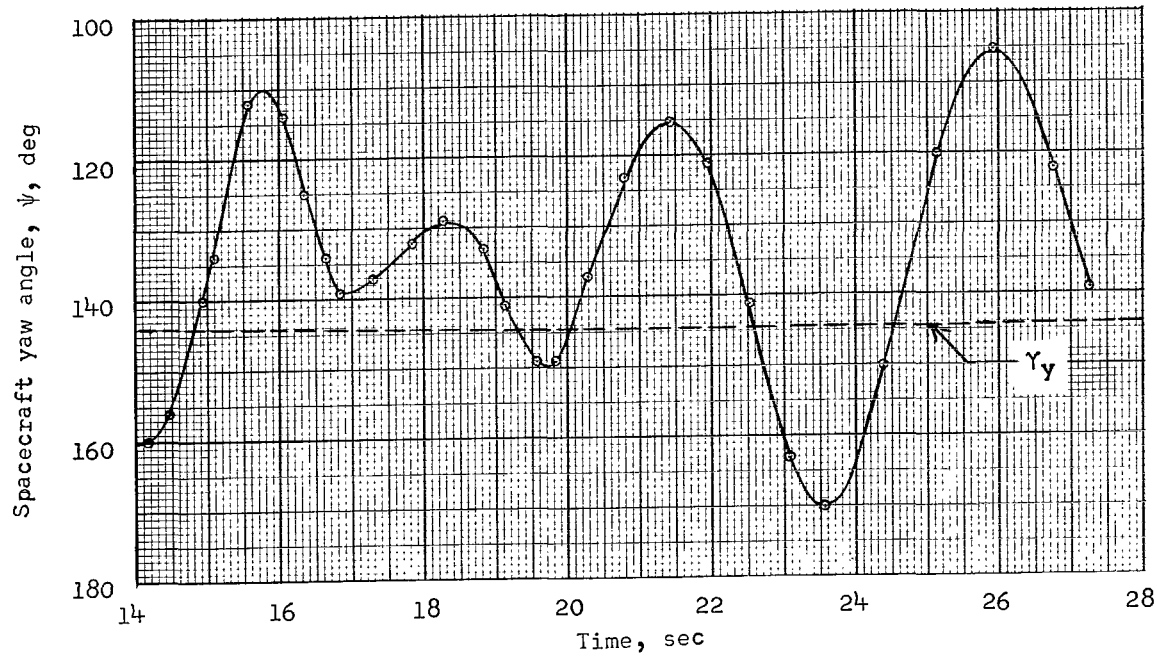

(b) Camera 2.

Figure 5.- Yaw-angle time history.

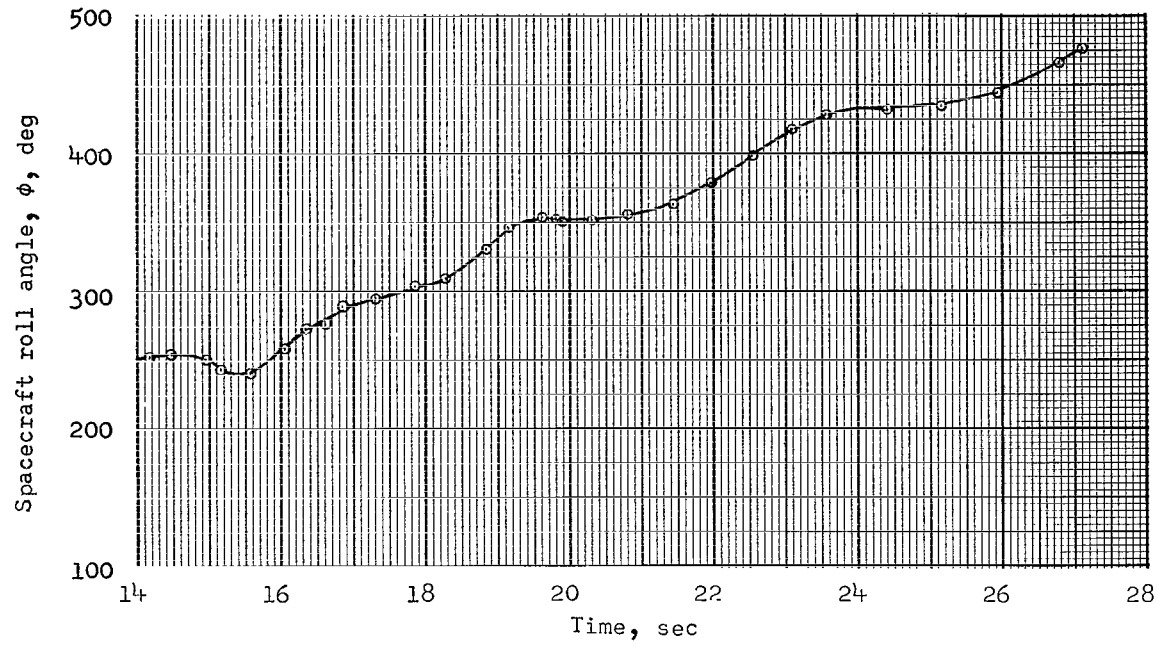

(a) Camera 1.

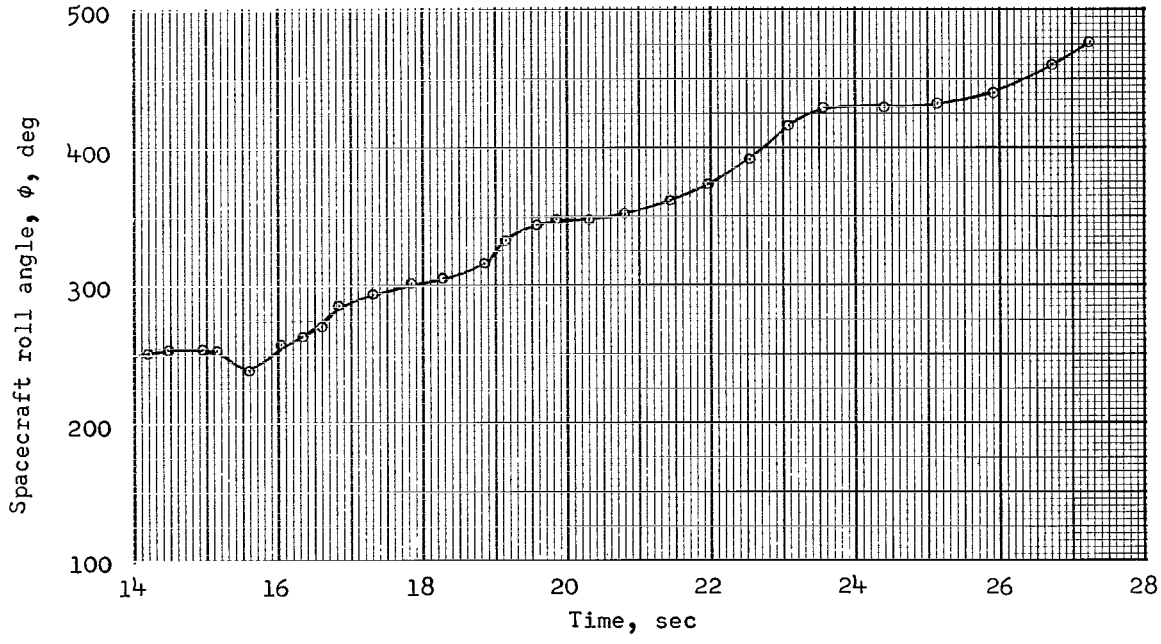

(b) Camera 2.

Figure 6.- Roll-angle time history.

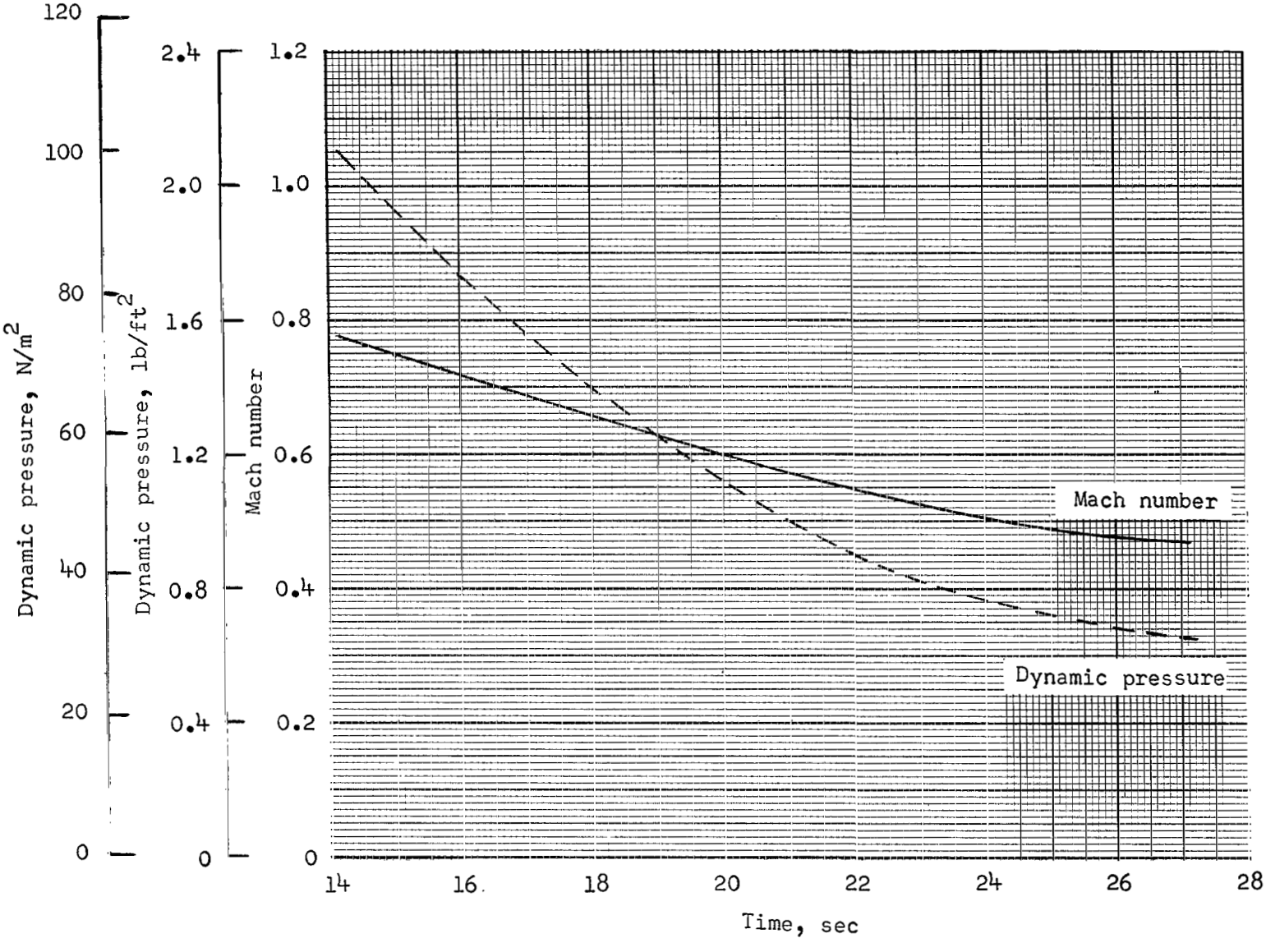

Figure 7.- Mach number and dynamic pressure history.

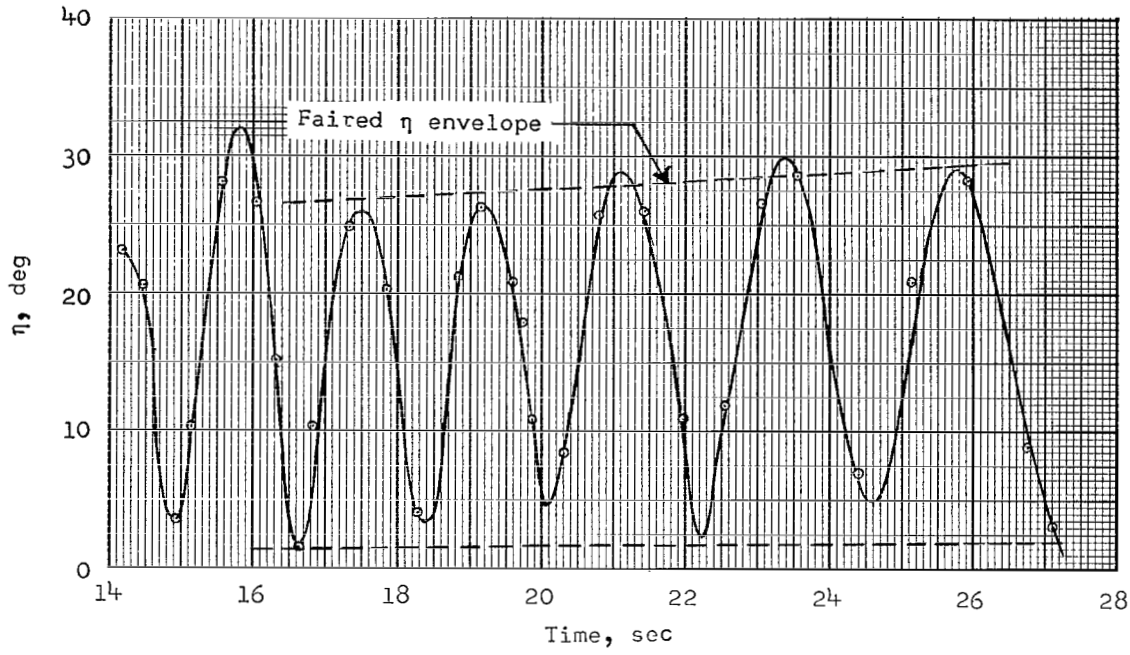

(a) Camera 1.

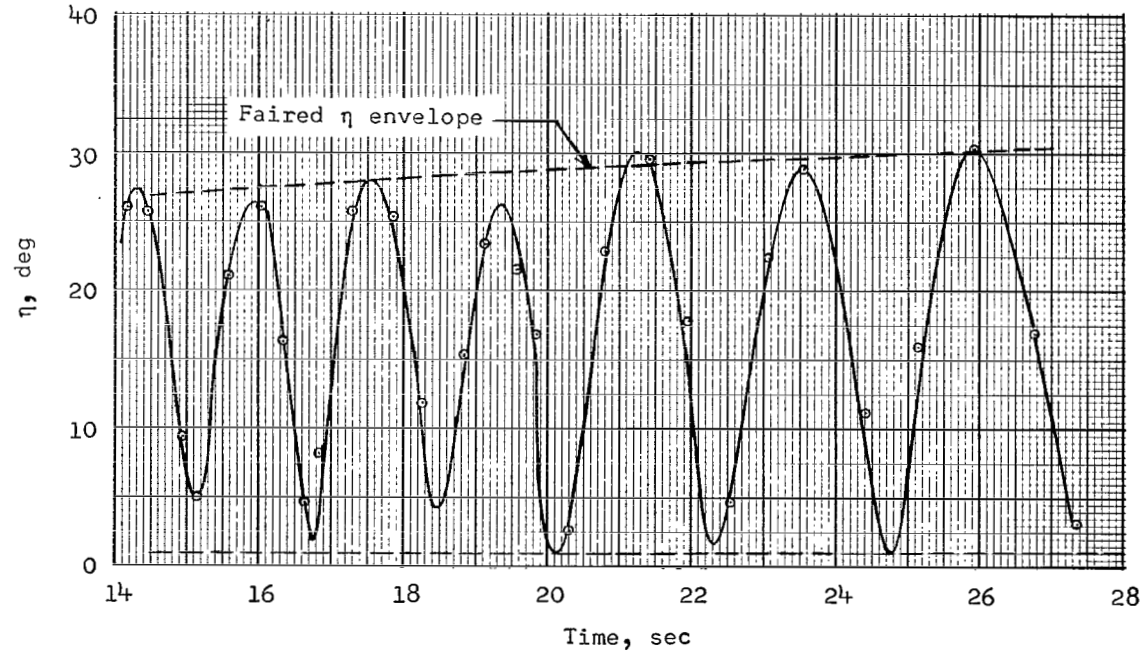

(b) Camera 2.

Figure 8.- Time histories of η from camera data.

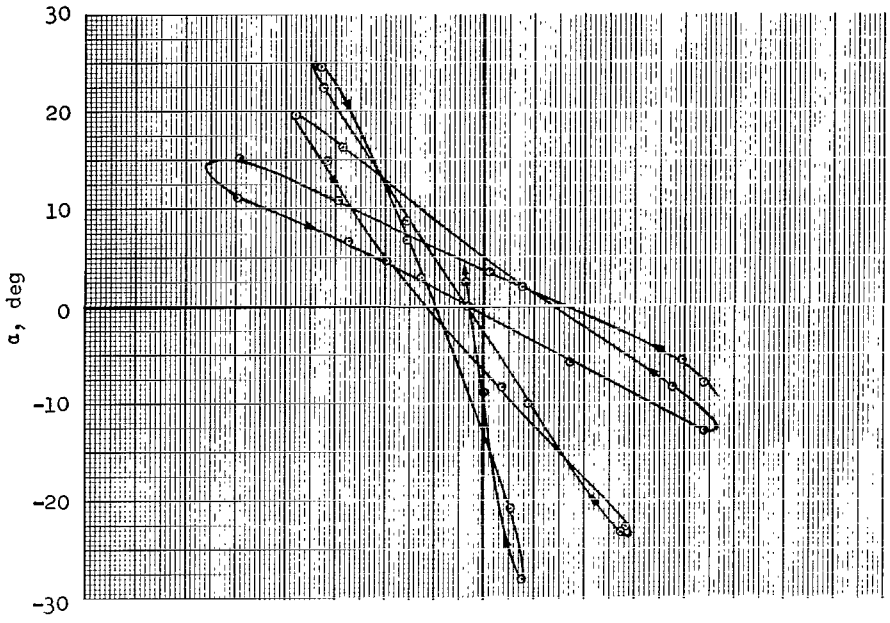

(a) Camera 1.

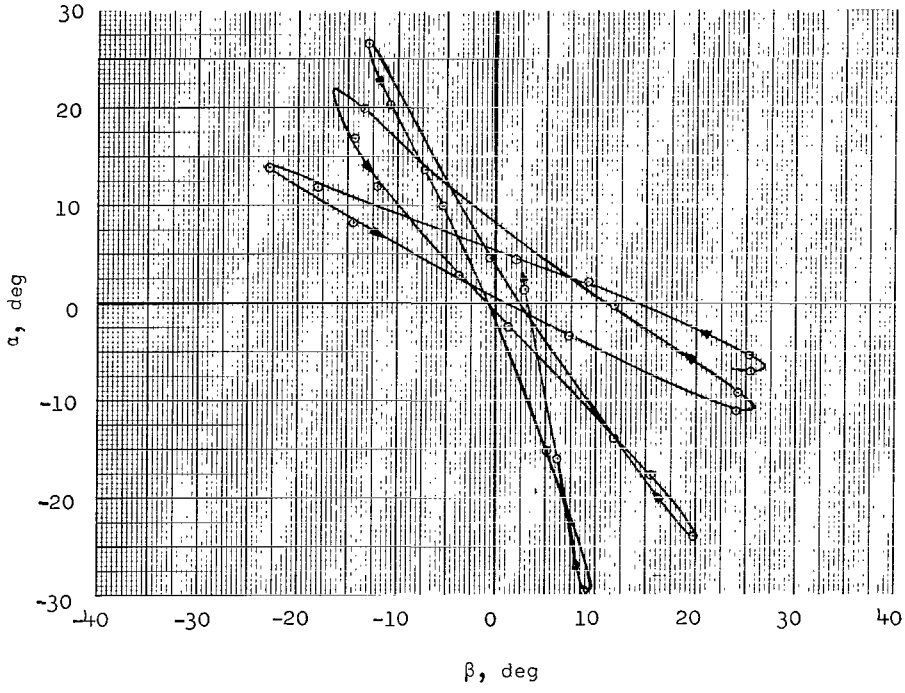

(b) Camera 2.

Figure 9.- Variation of α with β from camera data.

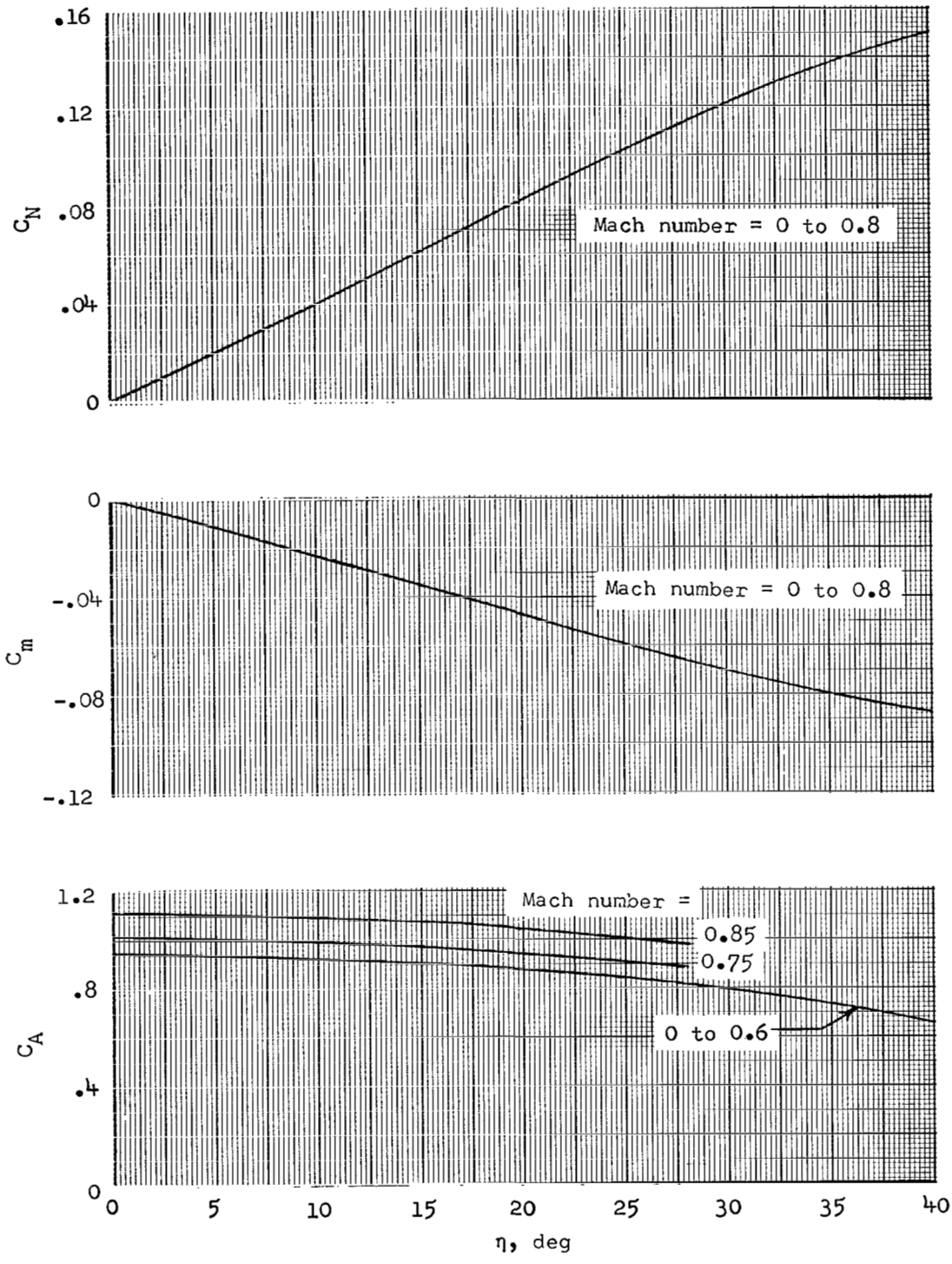

Figure 10.- Static aerodynamic coefficients.

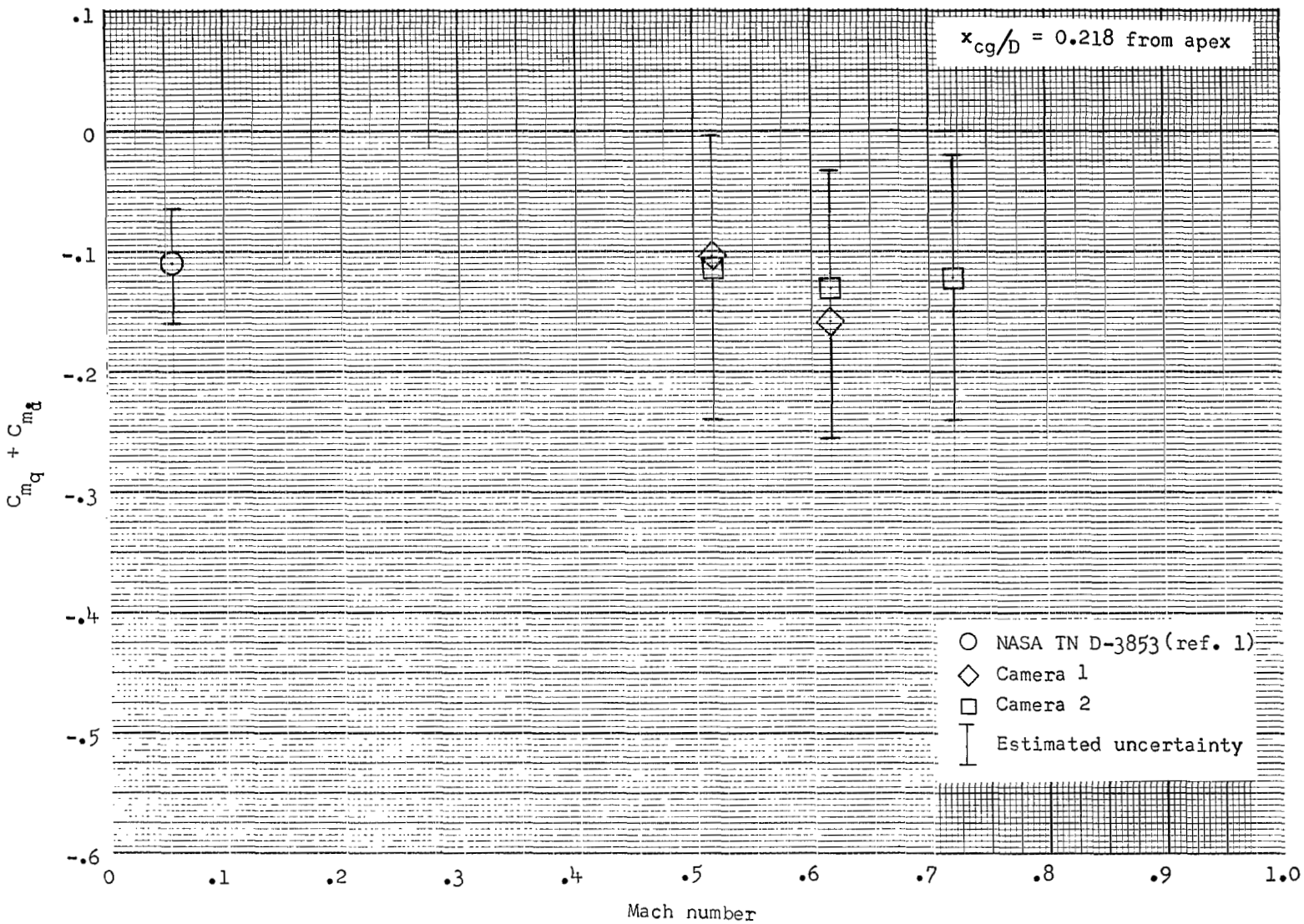

Figure 11.- Variation of $C_{m_q} + C_{m_{\dot{\alpha}}}$ with Mach number.

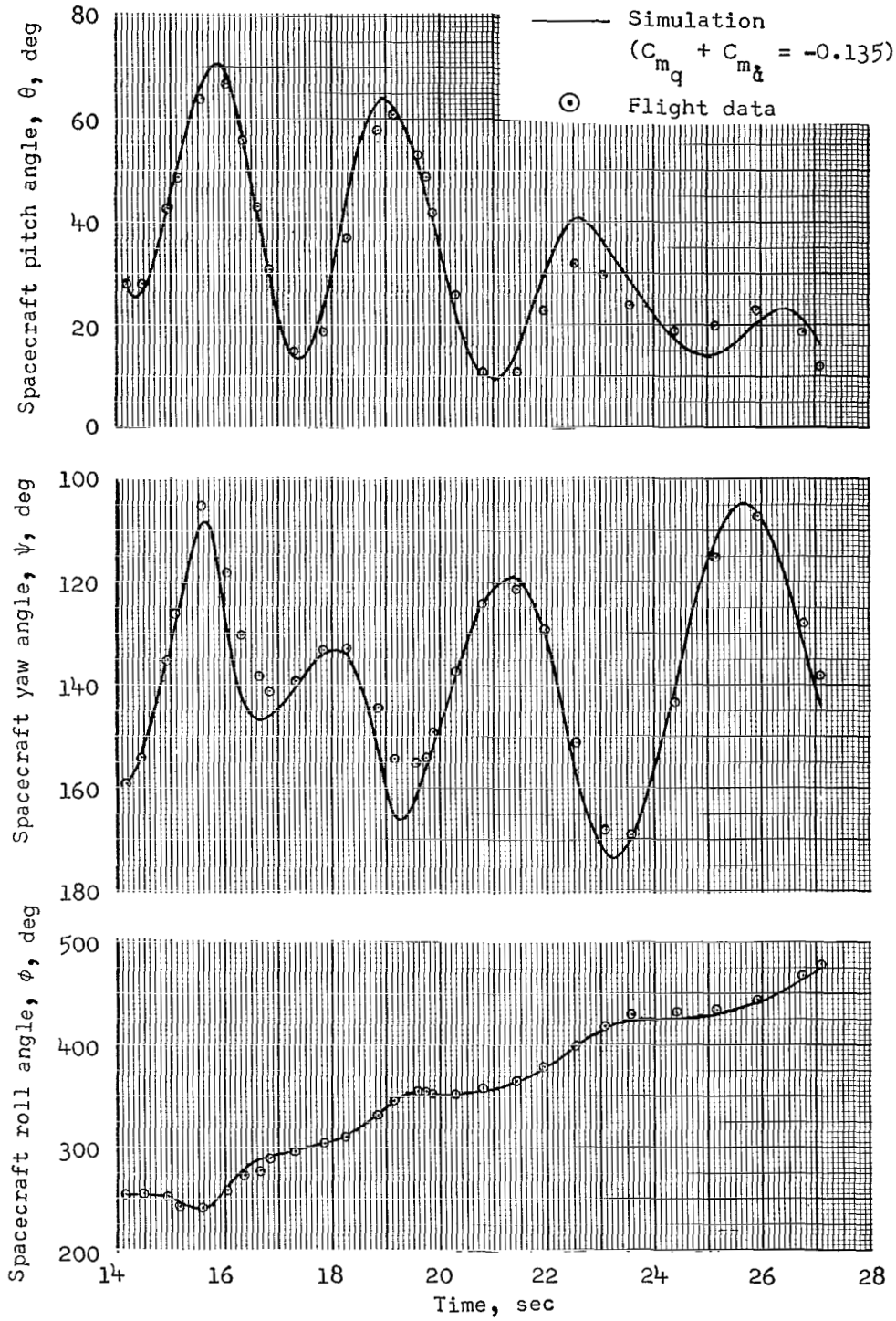

Figure 12.- Comparison of simulation and flight θ, ψ, and Φ time histories.

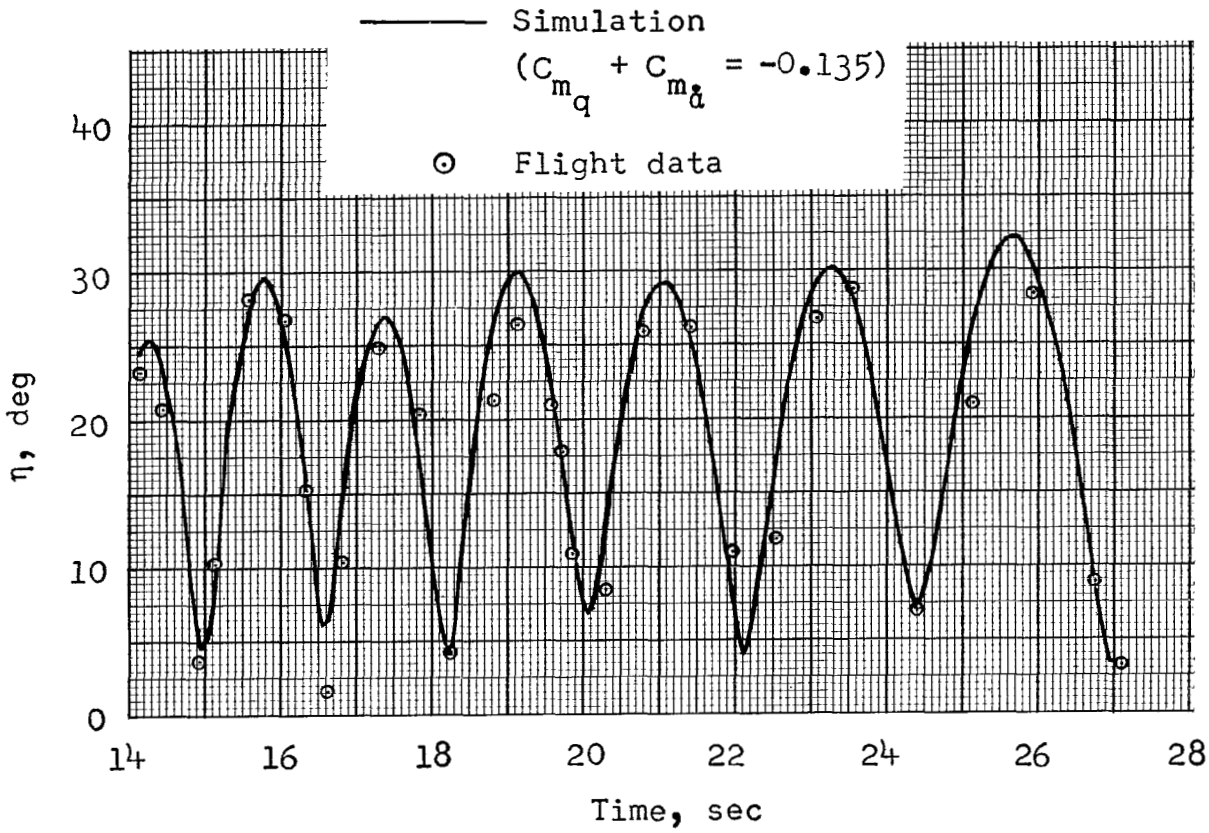

Figure 13.- Comparison of η time histories from simulation and flight data.

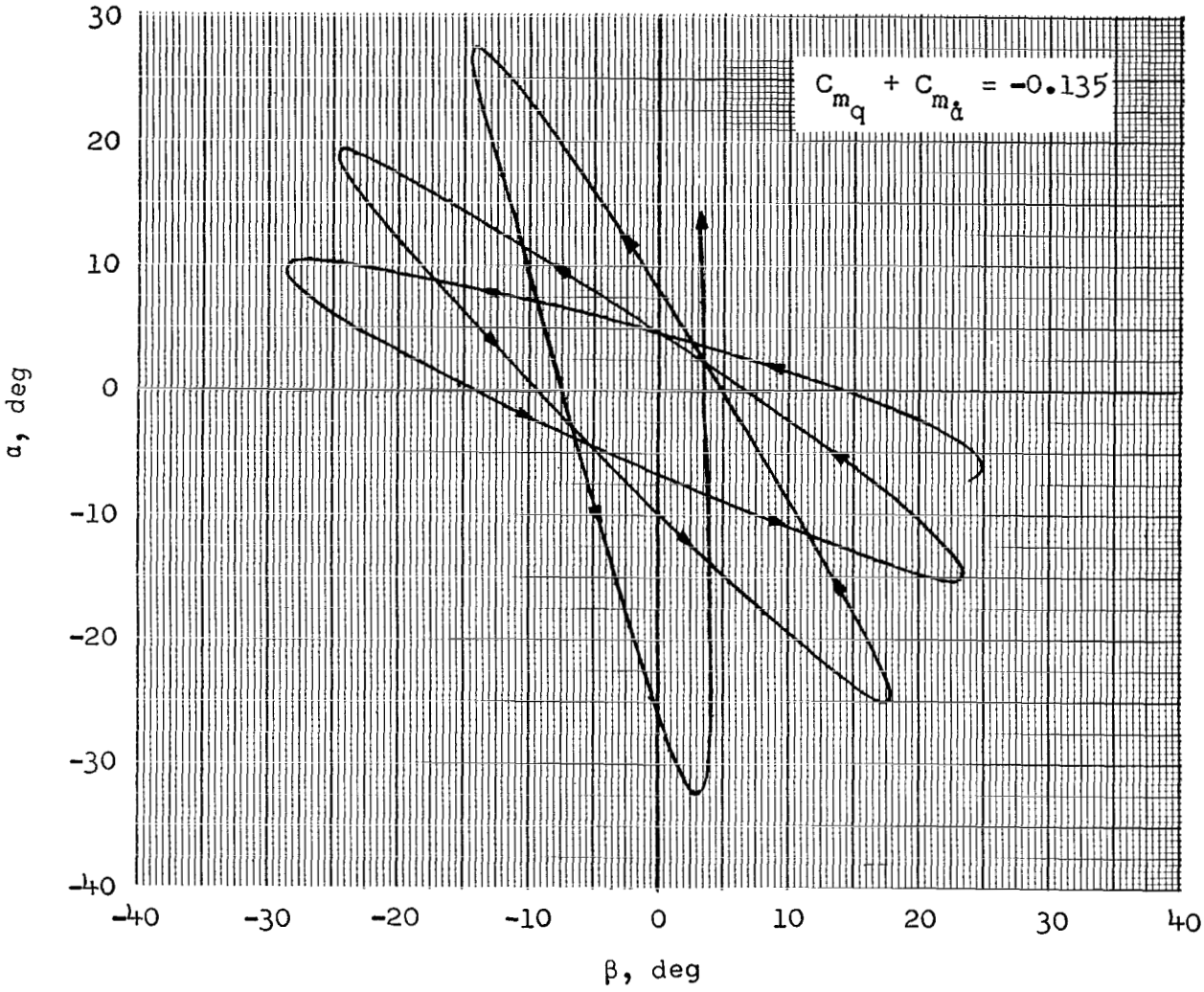

Figure 14.- Variation of α with β from simulation.

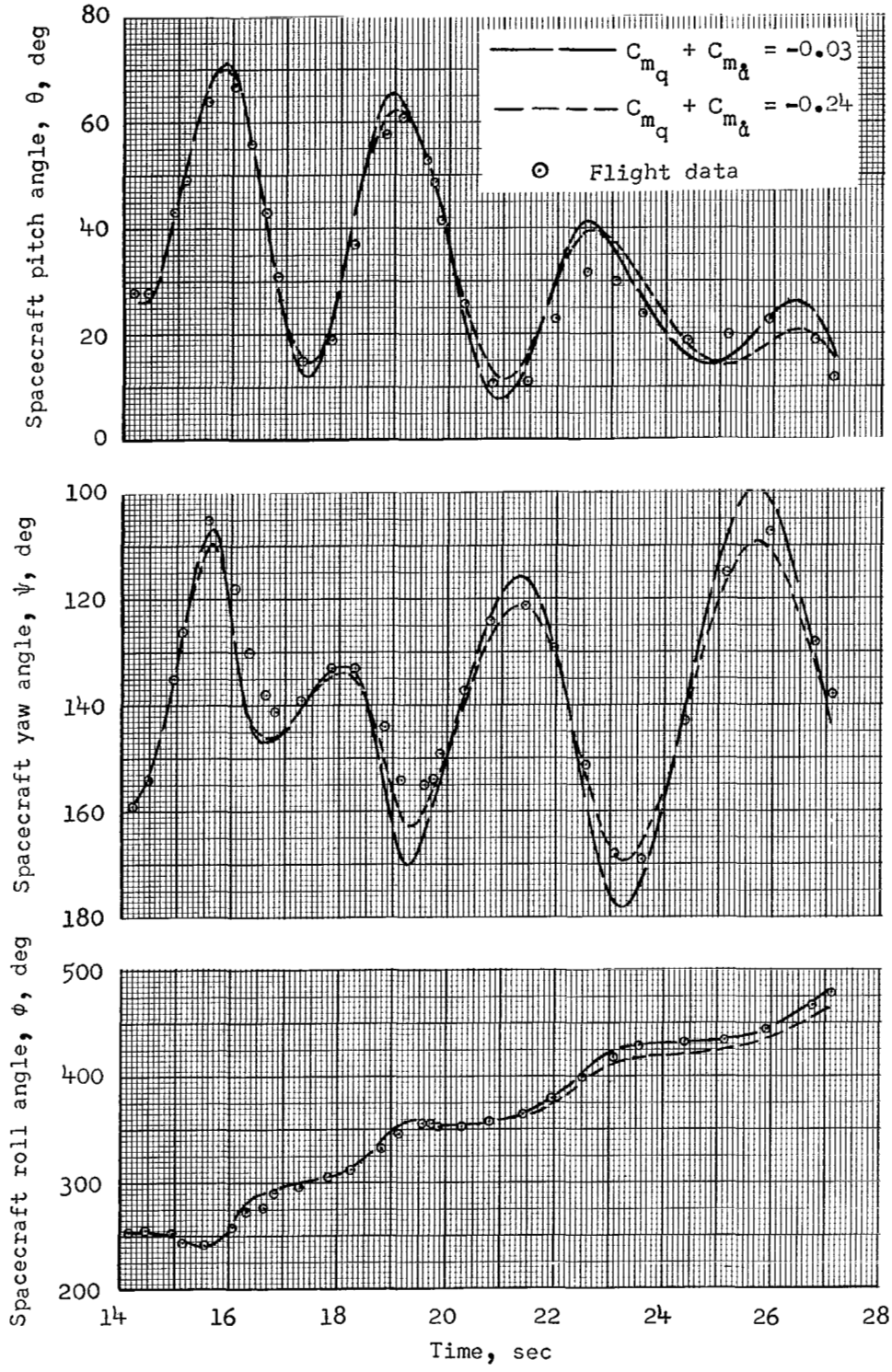

Figure 15.- Simulated θ, ψ, and Φ histories using $C_{m_q} + C_{m_{\dot{\alpha}}}$ accuracy limits.

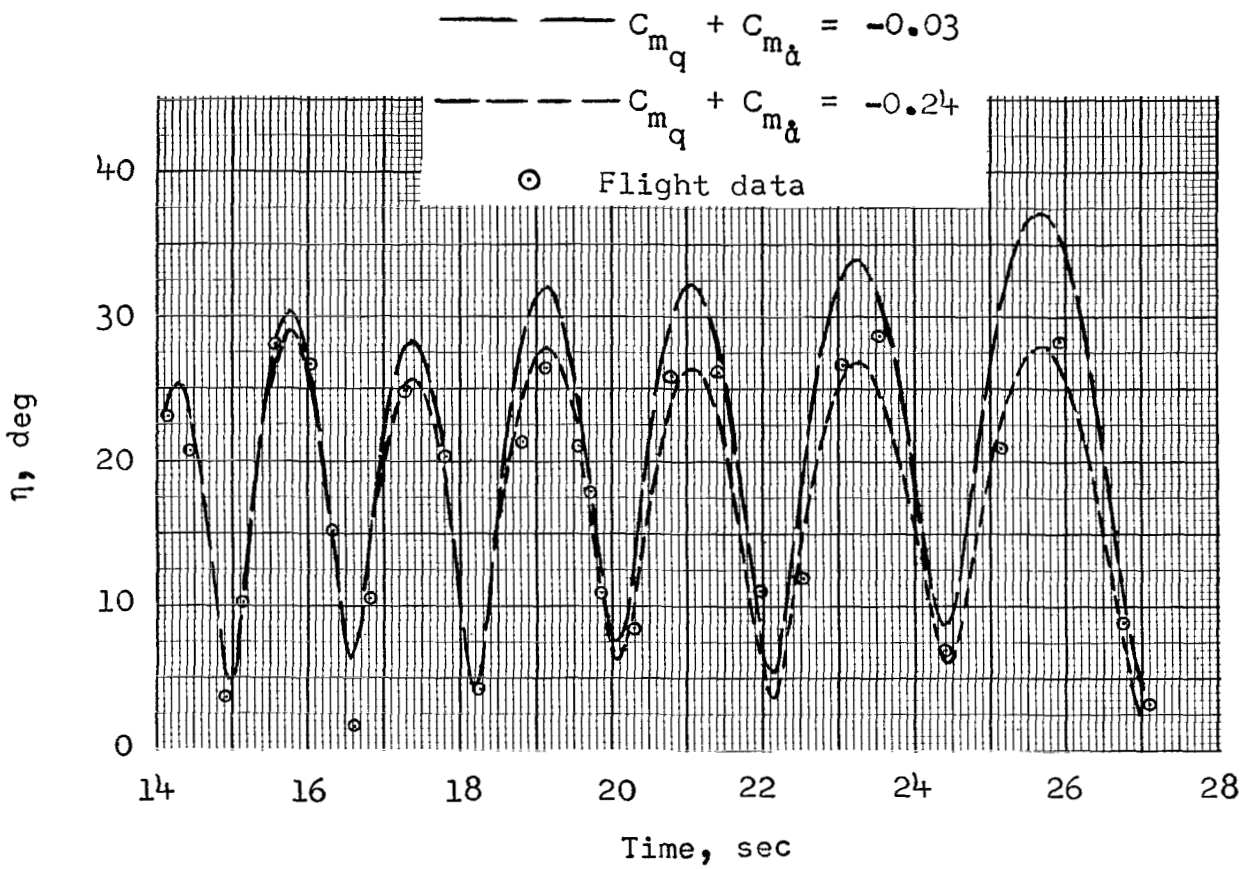

Figure 16.- Simulated η time histories using $C_{m_q} + C_{m_{\dot{\alpha}}}$ accuracy limits.